HHS Public Access

Author manuscript

Minerals (Basel). Author manuscript; available in PMC 2019 September 30.

Published in final edited form as:

Minerals (Basel). 2018 December ; 8(12): . doi:10.3390/min8120557.

Mineralogical Characterization and Dissolution Experiments in Gamble's Solution of Tremolitic Amphibole from Passo di Caldenno (Sondrio, Italy)

Ruggero Vigliaturo[1,*], **Giancarlo Della Ventura**[2,3], **Jessica K. Choi**[1], **Alessandra Marengo**[4], **Federico Lucci**[2], **Michael J. O'Shea**[1], **Ileana Pérez-Rodríguez**[1], **Reto Gieré**[1,5]

[1]Department of Earth and Environmental Science, University of Pennsylvania, Philadelphia, PA 19104-6316, USA; jesschoi@sas.upenn.edu (J.K.C.); michajo@sas.upenn.edu (M.J.O.); ileperez@sas.upenn.edu (I.P.-R.); giere@sas.upenn.edu (R.G.) [2]Dipartimento di Scienze, Università Roma Tre, Largo S. Leonardo Murialdo 1, I-00146 Roma, Italy; giancarlo.dellaventura@uniroma3.it (G.D.V.); federico.lucci@uniroma3.it (F.L.) [3]INFN Laboratori Nazionali di Frascati, Via E. Fermi 40, I-00044 Frascati/Rome, Italy [4]Dipartimento di Scienze della Terra, Università degli Studi di Torino, Via Valperga Caluso 35, I-10125 Torino, Italy; alessandra.marengo@unito.it [5]Center of Excellence in Environmental Toxicology, University of Pennsylvania, Philadelphia, PA 19104, USA

Abstract

In nature, asbestos is often associated with minerals and other non-asbestiform morphologies thought to be harmless, but not much is known about the potential toxic effects of these phases. Therefore, the characterization of natural assemblages should not be limited to asbestos fibers only. This paper combines a multi-analytical characterization of asbestos from Valmalenco (Italy) with data from dissolution experiments conducted in a simulated interstitial lung fluid (Gamble's solution), and a detailed dimensional study that compares the particle population before and after this interaction. The sample is identified as a tremolitic amphibole, exhibiting a predominance of fiber and prismatic habits at lower magnification, but a bladed habit at higher magnification. The results show that at different magnification, the dimensional and habit distributions are notably different. After the dissolution experiments, the sample showed rounded edges and pyramid-shaped dissolution pits. Chemical analyses suggested that a nearly stoichiometric logarithmic loss of Si and Mg occurred associated with a relatively intense release of Ca in the first 24 h, whereas Fe was probably redeposited on the fiber surfaces. A rearrangement of the more frequent habits

[*]Correspondence: ruggero.vigliaturo@gmail.com.

Author Contributions:

Conceptualization, R.V., J.K.C. and R.G.; Formal analysis, R.V.; Funding acquisition, G.D.V., I.P.-R. and R.G.; Investigation, R.V., G.D.V., J.K.C., A.M. and F.L.; Methodology, R.V., G.D.V., J.K.C. and A.M.; Supervision, R.G.; Writing—original draft, R.V., J.K.C., A.M. and M.J.O.; Writing—review & editing, R.V., G.D.V., J.K.C., A.M., F.L., M.J.O., I.P.-R. and R.G.

Conflicts of Interest: The authors declare no conflict of interest.

Supplementary Materials: The following are available online at http://www.mdpi.com/2075–163X/8/12/557/s1, Supplementary Materials S1: Dimensional distributions, Supplementary Materials S2: Gamble's solution concentrations.

and dimensions was recorded after the dissolution experiment, with a peculiar increase of the proportion of elongated mineral particles.

Keywords

asbestos; Gamble's solution; multi-analytical approach; fractal model; dissolution; mimicked biofluids; Valmalenco; medical mineralogy; asbestos regulatory use

1. Introduction

Exposure to asbestiform amphiboles can trigger several diseases, including asbestosis, squamous-, small-, and large-cell carcinoma, adenocarcinoma, and mesothelioma. Currently, there is no clear epidemiological evidence that non-asbestiform amphiboles (e.g., cleavage fragments) may lead to these malignancies [1], but the role of amphibole cleavage fragments needs to be determined and placed within the context of the toxicity of asbestos-like phases, even if it might play only a synergistic role with their fiber-shaped counterparts. Since "asbestos" is an inadequate and incomplete non-scientific term inherited from industrial and regulatory uses [2], it is important to provide details of all the phases, including their shapes and dimensional parameters, present in complex amphibole-bearing rocks or powders in order to assess their potential effect in disrupting normal physiological functions and homeostasis (e.g., iron homeostasis in cells).

This approach is even more important after evidence has become available that asbestiform minerals may not only induce fibrosis and malignancies, but also other diseases. One example is autoimmune disease, where an association between exposure and autoantibodies has been shown to exist [3]. While asbestosis and mesothelioma all over the world are immediately related to asbestos, the recognized cases of autoimmune disease are much rarer because of a lack of systematic investigation and sufficient available cohorts of study [4]. One of the rare case studies is Libby, Montana, where detailed mineralogical investigations have revealed that six amphiboles occur, namely: winchite, richterite, tremolite, magnesio-riebeckite, magnesio-arfvedsonite, and edenite. However, only tremolite is regulated as asbestos, and the exact identification of the different fiber compositions can be dependent on the data reduction method used or can vary among different laboratories [5].

Furthermore, recent studies show evidence that ingestion of asbestos fibers may lead to development of malignancies [6–9]. Yet, there is no study on the eventual contribution of other non-asbestiform amphiboles or mixed-habit powders to this possible disease pathway. The description of these recognized dangerous minerals as well as of minerals that are similar crystallochemically or in terms of their habit is important for the identification of geographic areas of potential risk and for understanding the transformation that occurs to the minerals during the interaction with the biosphere, which would help the medical community in describing the generation and development of these diseases.

In this paper, we describe the mineralogical characteristics of a metamorphic rock sample from Passo di Caldenno (Western Valmalenco, Northern Italy), which contains naturally occurring asbestos (NOA). NOAs are typical secondary mineral assemblages in mafic and

ultramafic rock sequences [10–14], where a wide range of geological processes, including shear deformation and fluid-rock interaction, may produce a considerable rock alteration and serpentinization, with formation of asbestiform amphiboles. The particle population will be described through several statistical parameters and by applying a fractal model over different magnification ranges, in an attempt to describe its wide variability in terms of dimensions and habit. The sample characterization has been conducted through a multi-analytical approach, and we will provide details on the dissolution of the bulk mineral powder in a simulated interstitial lung fluid by tracking the release of select elements and by recording the dimensional re-distribution of the amphibole particles.

Geological Setting

Passo di Caldenno (2517 m above sea level [m asl]) is located in the Central Alps (Sondrio province, Northern Italy), near the border of south-eastern Switzerland (Figure 1a). It is the northern termination of Monte Caldenno (2669 m asl) and the western limit of Valmalenco. The study area is geologically rather complex, as it is located at the boundary between the Penninic and Austroalpine nappes [15] (Figure 1b). The Penninic Malenco unit, the largest outcrop of ultramafic rocks in the Alps [16], is delimited by the Valtellina Valley to the south and the Engadine Valley to the north. These two valleys correspond to the regional structures of the Insubric Line (or Tonale Fault) and the Engadine Line, respectively (e.g., [16,17]). The Malenco unit is overlain by the Austroalpine nappes, which consist of gneisses, schists and phyllites associated with marbles, calc-schists and quartzite [18]. Despite the pervasive recrystallization phenomena resulting from the Alpine metamorphism, several lenses of pre-Alpine high-grade assemblages are preserved in the Malenco unit [17]. Penninic and Austroalpine nappes were intruded by Oligocene felsic plutons, including the 30–32 Ma Bergell granitoids (Masino-Bregaglia) and the Tonalite di Triangia intrusion (Figure 1b). Amphiboles have been reported to occur in all major mafic lithologies of the study area (e.g., [17,19]), including the following varieties: (i) ‘orthoamphibole’, pargasite, tschermakite, ‘hornblende’, and tremolite in gabbros, and (ii) magnesio-hornblende, cummingtonite, and tremolite in spinel peridotites. Secondary amphibole-bearing assemblages, however, occur as well, mostly in mafic and ultramafic rocks, but also in carbonates, within the contact aureole surrounding the Bergell pluton (e.g., [15,19]).

2. Materials and Methods

The sample was characterized using a multi-analytical approach combining: Visible-Light Microscopy (VLM), X-Ray Powder Diffraction (XRPD), Electron Probe Micro-Analysis (EPMA), μ-Raman Spectroscopy, Fourier-transform Infrared Spectroscopy (FTIR), BET surface area determination, laser diffraction, Field Emission Environmental Scanning Electron Microscopy (FE-ESEM) coupled with Energy-Dispersive X-Ray Spectroscopy (EDXS). Mineral dissolution in Gamble’s solution was tracked using Inductively Coupled Plasma-Optical Emission Spectrometry (ICP-OES). After the dissolution experiment, the remaining solid material was studied using FE-ESEM-EDXS.

2.1. VLM

The sample (≈15 × 5 cm) was examined as received (≈231 g of material) and broken into small pieces (1–3 cm across) using a hammer. These fragments were studied without further preparation using a Leica M165 C stereomicroscope (Leica Microsystems, Wetzlar, Germany) equipped with a Leica IC80 D camera (Leica Microsystems, Wetzlar, Germany) and an LED illumination system.

2.2. XRPD

Powder diffraction data were collected using a Scintag X1 diffractometer (ThermoFisher, Waltham, MA, USA) with Cu-Kα_1 radiation (λ = 1.54055 Å, 40 mA, 45 kV), fixed divergence slits, and a Peltier-cooled Si (Li) detector with a resolution of <200 eV. A divergent slit width of 2 mm and a scatter-slit width of 4 mm were employed for the incoming beam, whereas a receiving slit width of 0.5 mm and scatter-slit width of 0.2 mm were used for the diffracted beam. Data were collected in step-scan mode in the 2–70° 2θ range, with a step size of 0.05° 2θ, and a counting time of 3 s/step.

2.3. EPMA

Amphibole compositions were obtained by combining wavelength-dispersive EDXS techniques using a CAMECA SX50 electron microprobe (CAMECA, Gennevilliers, France) at “Centro di Studi per il Quaternario e l’Evoluzione ambientale—CNR” (Rome). Analytical conditions were: 15 keV accelerating voltage, 20 nA beam current, 5 μm beam size and 100 s counting time. Data reduction was made using the ZAF4/FLS software (standard version) by Link Analytical (Oxford, UK). Compositions were determined relative to natural and synthetic standards.

2.4. μ-Raman and FTIR Spectroscopy

μ-Raman analyses on untreated samples were carried out employing a confocal Horiba-Jobin Yvon LabRam HRVIS (HORIBA, Ltd., Kyoto, Japan), equipped with a motorized x-y stage and connected to a BX41 Olympus microscope (Olympus Corporation, Tokyo, Japan). The backscattered Raman signal was collected with a 50× objective, and Raman spectra were obtained for non-oriented crystals. The 532 nm line of a He-Ne laser was used as excitation source, with the laser power (80 mW) controlled by a series of density filters. Spectra were collected in the region between 100 and 4000 cm^{-1}, with a hole aperture of 200 μm, diffraction gratings of 1800 g/mm, and integration times of 10 to 40 s, for 10 accumulation cycles. The lateral and depth resolutions were approximately 2 and 5 μm, respectively. The system was calibrated against the Stokes Raman signal of pure Si at 520 cm^{-1} before each experimental session. Spectral manipulation, such as baseline adjustment, smoothing and normalization, were performed with the Labspec 5 software package (version 5.64.15, HORIBA, Ltd., Kyoto, Japan) (Horiba Jobin Yvon GmbH 2004, 2005). Band-component analysis was undertaken using a Lorentzian function (Fityk software package (version 1.3.1), [20]).

The chemical composition of the same fragments characterized by μ-Raman was further determined using a JEOL JSM IT300LV (JEOL, Ltd., Akishima, Tokyo) scanning electron microscope (SEM) equipped with an Oxford Inca Energy 200 EDXS microanalysis system

(Oxford Instruments plc, Abington, UK), a Pentafet detector and an ultrathin window (Z > 5). All spectra were obtained at an accelerating voltage of 15 kV, a working distance of 10 mm and an exposure time of 60 s. Primary standardization was performed on SPI Supplies and Polaron Equipment analytical standards, whereby daily standardization was performed against a high-purity metallic Co standard.

Powder FTIR spectra were collected using a Nicolet iS50 FTIR spectrometer (ThermoFisher Scientific, Waltham, MA, USA) equipped with a DTGS detector and a KBr beam splitter; the nominal resolution was 4 cm^{-1}, and 64 scans were averaged for each sample and for the background. Samples were prepared using the conventional KBr pellet technique: one disk was prepared for the investigation of the OH-stretching region (4000–3000 cm^{-1}) by mixing 7 mg of amphibole powder with 150 mg of KBr; a second disk was prepared by mixing 0.5 mg of amphibole powder with 150 mg of KBr for analysis of the framework modes region (<1200 cm^{-1}). In addition, a single-crystal spectrum in the OH-stretching region was collected using a Bruker Hyperion 3000 FTIR microscope (Bruker Corporation, Billerica, MA, USA) with a beam dimension of 20 μm. The resulting pattern was virtually identical to the powder pattern.

For all the following analyses, the sample fragments were initially crushed into mm-wide crystals. This material was then ground by hand for 5 min in 2-propanol using an agate pestle and mortar to obtain a powder. As described in the following FE-ESEM-EDXS section, the sample material was further investigated on a larger scale, as mm-sized crystals and cm-sized rock fragments, to complement the morphological information obtained through VLM.

2.5. BET Surface Area Analysis

Once the powder was dry, 2.6476 g of the sample were loaded in a tube and conditioned under N_2 flow at 100 °C. The BET specific surface area ($m^2 \cdot g^{-1}$) was then determined using a Micromeritics TriStar 2000 instrument (Micromeritics, Norcross, GA, USA) and N_2 as probe gas.

2.6. Laser Diffraction

The particle-size distribution of the powdered material was analyzed with a Beckman-Coulter LS 13 320 particle-size analyzer (Beckman Coulter Inc., Brea, CA, USA). For this purpose, ~0.5 g of sample was dispersed in distilled water and inserted in the instrument.

2.7. FE-ESEM-EDXS

A FEI Quanta 600 FEG Mark II Field Emission SEM (FEI Company, Hillsboro, OR, USA) was used to obtain detailed information on the starting material. We studied (i) the morphology of the sample subsequent to the hammering in a 3 cm-sized fragment, and (ii) the hand-ground sample to determine the habit of individual, fractured particles, their dimensional distribution, and track the chemical transformation before and after the interaction with the mimicked interstitial lung fluids. Each specimen was mounted on a 12.7 mm SEM stub by using conductive carbon tabs. The SEM was set to environmental mode with a voltage of 15 kV and a chamber pressure of 0.38 torr. Variable spot dimension was

used to optimize imaging or chemical analyses (size 3 and 6, respectively). All images shown here were taken in secondary electron (SE) mode.

The size-distribution and morphological studies were conducted under the same conditions, but with a voltage of 30 kV and a magnification of $10^2\times$, $10^3\times$ and $10^4\times$ to cover three orders of magnitude in our measurements and to obtain three separate dimensional distributions. The descriptive statistics show the parameters that are commonly used for the regulatory descriptions of fiber populations, i.e., their length (L), width (w), and aspect ratio ($\boldsymbol{\beta}=\boldsymbol{L}/\boldsymbol{w}$), as well as additional parameters, such as the real area (measured), the calculated area (the area given by $\boldsymbol{L}\cdot\boldsymbol{w}$), the dimension "$s$" which is given by $\sqrt{A_{real}}$, and the aerodynamic equivalent diameter (D_{ae}). This dimensional study was performed on both the hand-ground starting material and the material after it had interacted for 168 h with Gamble's solution.

The dimensional distributions obtained for the starting material were modelled by applying a fractal model. The rationale of our choices is explained in the corresponding section. In general, the applied procedure was as follows: (i) removal of outliers, (ii) definition of the optimal binning by qualitatively comparing the Scott's and Freedman-Diaconis's methods, (iii) discretization of the distribution using the K-means algorithm, (iv) power-law fitting of the experimental distribution, and (v) calculation of the fractal dimension "D".

The powdered sample was morphologically and chemically characterized again after it had been exposed for 168 h to Gamble's solution. In particular, we studied the $\frac{Mg}{Si}$, $\frac{Ca}{Si}$, and $\frac{Fe}{Si}$ atomic ratios in the bulk of both the powdered sample before the interaction and the powdered sample after 168 h of interaction with Gamble's solution, as well as in Gamble's solution itself.

2.8. ICP-OES

The release of elemental species from the powdered sample was investigated by dissolution experiments using Gamble's solution (simulating lung fluid), following previous experimental approaches but with a few modifications [21,22]. The modified Gamble's solution was composed of ($g\cdot L^{-1}$): $MgCl_2\cdot 6H_2O$, 0.203; NaCl, 6.019; KCl, 0.298; Na_2HPO_4, 0.126; Na_2SO_4, 0.063; $CaCl_2\cdot 2H_2O$, 0.368; $NaC_2H_3O_2\cdot 3H_2O$, 0.952; $NaHCO_3$, 2.604; and $Na_3C_6H_5O_7\cdot 2H_2O$, 0.097, brought to a final pH of 7.4. Subsequent to the preparation of Gamble's solution, the powdered sample was added to the solution to a final concentration of 1.25 $mg\cdot mL^{-1}$. This suspension was mixed homogenously using a magnetic stir bar while dispensing into 10 mL batch reactors. Additionally, negative controls containing Gamble's solution only were also prepared. All batch reactors were prepared in triplicate and subsequently incubated at 37 °C to mimic human body conditions. Ultimately, we prepared a total of 48 batch reactors, each containing 10 mL of suspension.

The entire contents of three batch reactors for each of our two experimental conditions (Gamble's with powdered sample and the negative control, for a total of 6) were sacrificed per time point at 0, 0.5, 1, 12, 24, 48, 96, and 168 h after dispensing. At each time point, the 10 mL suspensions from all 6 batch reactors were centrifuged at 2000× g for 5 min to

concentrate the powdered sample into a pellet. The supernatants containing just the Gamble's solution were decanted into clean tubes and stored at 4 °C until further processing by ICP-OES as outlined below. The pellets containing the powdered samples were subsequently resuspended in milliQ water (18.2 Ω· cm, 22 °C), transferred into larger 50 mL Falcon tubes, then spun again to wash the mineral phases. This washing step was repeated once more before the water was carefully removed using a serological pipet.The pellets collected at 168 h were then dried before FE-SEM-EDXS analysis as described above.

The Gamble's solutions from all 48 batch reactors were analyzed by ICP-OES for specific elements using a Spectro Genesis instrument equipped with a Modified Lichte nebulizer and 25 mm axial plasma torch. The Gamble's solutions were diluted down 1:100 in clean milliQ water before analysis. The elemental concentrations were quantitatively determined for Si at a wavelength of 251 nm, Mg at 288 nm, Ca at 315 nm, Fe at 259 nm, and Al at 308 nm. The elemental dissolution rate is given by $\frac{d(El)}{dt}$, where "*El*" is the specific element concentration in solution (mol·g^{-1}), "*t*" the considered reaction time (s), and subsequently normalized to the surface area (m^2·g^{-1}).

3. Results

3.1. Naked-Eye and VLM Description of the Sample

The hand specimen is mainly composed of mm-sized aggregates of green, elongated, prismatic crystals, which typically exhibit a columnar habit or, more rarely, a bladed morphology. Some tabular greenish-black crystals are visible among the aggregates. Occasionally, fibrous and silky aggregates can be found, of which the parallel and well-elongated thin crystals resemble asbestiform fibers.

At VLM scale, some darker columnar crystals are visible, as well as diffuse vivid green aggregates, which do not show any preferential orientation (Figure 2a). The columnar habit of dark green to black crystal aggregates is well defined and recognizable at this scale, but streaking parallel to the elongation axis of the crystals points to the presence of a possible asbestiform morphology at smaller scale (Figure 2b). The presence of grey to light green fibers in both random and parallel orientations is visible at higher magnification (Figure 2c,d). The luster is mostly vitreous for columnar and bladed crystals (Figure 2a,b) and silky for asbestiform fibers (Figure 2c,d).

3.2. XRPD

The XRPD pattern collected for the studied sample could be fully indexed in the *C*2/*m* space group. Refined cell dimensions were (in Å): a = 9.832 (1), b = 18.065 (4), c = 5.273 (1), β (°) = 104.76 (2), V (Å^3) = 905.7 (2), consistent with literature data for amphiboles in the tremolite-actinolite series, see [23]. The XRPD pattern further revealed the presence of a very small amount of chlorite (2 wt. %) as accompanying phase.

3.3. EPMA

Microchemical data (average of 12 individual point analyses) are given in Table 1; crystal chemical formulae were calculated according to the 13-CNK scheme (e.g., [24]) by using

the ACES2013 excel spreadsheet [25]. The examined amphibole is characterized by a very low Al_2O_3 content (<0.54 wt. %), but high CaO (12.58–13.74 wt. %) and MgO (20.58–21.62 wt. %) contents and thus belongs to the calcic group [26]. More specifically, by considering that the atomic ratio [Mg/(Mg + Fe2+)], i.e., #Mg, ranges from 0.86 to 0.90, and that Si > 7.85 apfu (7.85–7.96 apfu), the composition of the sample lies at the stoichiometric boundary between actinolite and tremolite [26–28], as shown in Figure 3. Therefore, we will use below the term *tremolitic amphibole* when generally referring to the sample.

3.4. μ-Raman and FTIR Spectroscopic Observations

The μ-Raman spectra were collected on dark green columnar crystal aggregates (Figure 4a,b). Figure 4c shows a representative Raman spectrum in the ranges 100–1200 and 3000–4000 cm^{-1}. The spectrum presents, in the lattice mode regions (<1200 cm^{-1}), a very strong peak at 673 cm^{-1}, with additional bands at 740, 750, 932, 1030, 1059, and 1070 cm^{-1}. In the < 600 cm^{-1} range, the following peaks have been observed: 120, 178, 222, 370, and 392 cm^{-1}, with weak bands at 160, 230, 247, 289, 307, 331, 351, 415, 487, 514, and 534 cm^{-1}. The observed patterns are in accordance with the data reported for tremolite and actinolite by Rinaudo et al. [30] and Apopei and Buzgar [31], respectively.

The powder FTIR spectrum collected in the OH-stretching region (Figure 5a) shows three well-resolved components at 3672, 3659 and 3643 cm^{-1}, which can be assigned to different combinations of Mg and Fe^{2+} at the *M*(1,3) sites of the amphibole structure [23,32].

According to several papers on amphibole spectroscopy (e.g., [23,32]), the relative intensities of the four components in the IR spectrum of a Mg-Fe^{2+}-amphibole are directly correlated to the relative amounts of the two substituting cations at the *M*(1,3) octahedra. The spectrum of Figure 5a has thus been decomposed into single Gaussians following the procedure discussed by Della Ventura [32], such as to derive the integrated intensities of the observed peaks. From these data, the amount of Fe^{2+} at *M*(1,3) was calculated at 0.58 apfu, in excellent agreement with the EPMA-derived value given in Table 1. The spectrum collected at wavenumbers <1200 cm^{-1} (Figure 5b) shows intense bands in the 1200–800 cm^{-1} range (region 1: [33]). The bands located at 1102, 1055, 996, 951, and 920 cm^{-1} can be assigned to lattice Si–O–Si and O–Si–O anti-asymmetric stretching vibrations. Weaker bands are present in the 800–600 cm^{-1} range (region 2: [33]); these are due to Si–O–Si symmetric stretching, chain deformation, and OH librational modes. Finally, intense bands are present at wavenumbers <650 cm^{-1} (507 and 463 cm^{-1}, with shoulders at 538 and 445 cm^{-1}), where a mixture of T–O and M–O bending modes occur. The collected pattern is almost identical to the one recently given for reference tremolite and actinolite [23], again in agreement with the composition of the sample studied here.

3.5. BET Surface Area Results

The standard multi-point (11-point analysis for nitrogen) BET surface area was determined at 0.4786 ± 0.0104 $m^2 \cdot g^{-1}$.

3.6. Particle-Size Distribution

The laser diffraction data for the powdered sample reveal a poorly sorted, bimodal particle-size distribution (Table 2).

3.7. Morphology as Observed by FE-ESEM for the Powdered Starting Material

Low-magnification morphological observations of a cm-sized fragment document that fiber morphology is predominant and that fibers in parallel arrangement are the basic units that form columns (Figure 6a). These fibers appear slightly curved and randomly oriented at fracture boundaries and apices (Figure 6b,d). Even the regions in which the mineral has a bladed or prismatic shape are made of individual asbestiform fibers (Figure 6c,d).

3.8. Dimensional Results Obtained by FE-ESEM for the Powdered Starting Material

Table 3 summarizes the values of all the considered dimensional parameters, separated according to magnification ($10^2\times$, $10^3\times$, $10^4\times$). At each of these magnifications, a total of 150 particles were measured. The real area (A_{real}) was measured directly on the pictures, whereas the calculated area (A_{calc}) was obtained by multiplying the measured L and w values (in µm). The ratio between these two areas is indicative of the deviation from a rectangular shape of the measured particle: when the A_{real}/A_{calc} value is close to 1.00, a particle has a squared morphology, whereas bladed particles with highly irregular boundaries typically show lower A_{real}/A_{calc} values. The dimensional parameter "s" does not depend on the shape of the particles [34] and simply corresponds to $\sqrt{A_{real}}$. The mean aerodynamic diameter (D_{ae}) was calculated using the simplified Equation [35]:

$$D_{ae} = w\sqrt{\left(\frac{1}{\frac{2}{9}\left(\frac{1}{(\ln(2\beta)-0.5)}\right)+\frac{8}{9}\left(\frac{1}{(\ln(2\beta)+0.5)}\right)}\right)\left(\frac{\rho_p}{\rho_0}\right)} \quad (1)$$

in which w is the particle width (µm), β is L/w, ρ_p is the particle density (g/cm^3), and ρ_0 is the unit density (1.00 g/cm^3).

The overall proportions of different habits in the studied particle population at different magnifications are summarized in Table 4. The definition of the different habits was made following Veblen and Wylie [36].

Elongated mineral particles (EMPs) are defined by the National Institute for Occupational Safety and Health (NIOSH) [37] as structures longer than 5 µm and with a defined aspect ratio equal to, or larger than, 3:1. Of the particles measured at $10^2\times$ and at $10^3\times$, 54.00% and 47.33% can be classified as EMPs, respectively, whereas only 2.00% of the measured particles are EMPs at $10^4\times$ (see full dimensional dataset and additional graphical representation in the Supplementary Materials, S1). This distinctly lower proportion of EMPs at the highest magnification results from particles being shorter than 5 µm.

3.9. Fractal Model from FE-ESEM Data Obtained for the Powdered Starting Material

A fractal model was applied to the length dataset for each magnification ($10^2\times$, $10^3\times$, and $10^4\times$) of the powdered sample. Since this dataset generated a highly right-skewed distribution for all three magnifications, we investigated it for outliers by applying a double Grubb's test after normalization of the data. The normalization consisted of transforming the right-skewed distribution of L into a Gaussian distribution by applying a logarithm to the starting dataset. The Grubb's test was then applied to the normalized dataset to remove real outliers, but not those outliers that are a consequence of a highly right-skewed distribution. The detected real outliers were then removed from the starting dataset. The optimal binning was calculated using both Scott's and Freedman–Diaconi's methods. Scott's method has been selected because the higher number of bins calculated through Freedman-Diaconis's method led to an increase in the noise of the distributions. The centroids of the classes were generated by discretization using the K-means algorithm. The smallest bin was arbitrarily removed from the results, as recommended by Wylie [38]. In Figure 7, we compare the logarithmic plots for L obtained for the three magnifications and fitted using power-law functions. The fractal dimensions obtained were as follows: $D = 2.59 \pm 0.35$ at $10^2\times$, $D = 2.35 \pm 0.24$ at $10^3\times$, and $D = 2.19 \pm 0.25$ at $10^4\times$.

3.10. ICP-OES Data from Dissolution Experiment

Data for elemental release from the powdered tremolitic amphibole sample after interaction with Gamble's solution are given in Table S2 (Supplementary Materials). We specifically monitored the release of Si, Mg, Ca, Fe, and Al into the aqueous phase over time, since these elements were found as important components of the studied amphiboles (Table 1) and because of their potential in the disruption of the biological environment (see the discussion section).

Silicon and Mg were released in a logarithmic fashion, as documented by the substantial increases in their concentrations in the solution during the first 48 h (Figure 8a). Subsequently, the concentrations of Si and Mg remained relatively constant (Figure 8a–Supplementary Materials S2). The dissolution rate of Si in the first 48 h was calculated at $1.21 \times 10^{-12} \pm 1.13 \times 10^{-13}$ mol·m^{-2}·s^{-1} ($R^2 = 0.92$), which is statistically identical to the Mg dissolution rate calculated at $1.24 \times 10^{-12} \pm 2.47 \times 10^{-13}$ mol·m^{-2}·s^{-1} ($R^2 = 0.84$).

A considerable release of Ca was observed during the first 24 h of the experiment ($3.51 \times 10^{-12} \pm 2.05 \times 10^{-13}$ mol·m^{-2}·s^{-1}, $R^2 = 0.97$), but the Ca concentration in Gamble's solution subsequently decreased again (Figure 8b). No release of Al from the starting material was detected, and only very small amounts of Fe were released (Supplementary Materials S2).

At the end of the dissolution experiments, i.e., after 168 h of interaction with Gamble's solution, we also determined the overall elemental ratios in the remaining bulk solid material in order to compare the same ratios in the starting material and in Gamble's solution (Table 5). The total error given in the following tables was calculated for each variable as:

$$\Delta X_{total} = \sqrt{\Delta X_{systematic} + \Delta X_{statistical}} \quad (2)$$

3.11. Morphology as Observed by FE-ESEM for the Material After Dissolution Experiment

The release of essential components from the sample during interaction with Gamble's solution is reflected by morphological changes, which resulted from the exposure. FE-ESEM observations performed on more than 100 particles provide evidence for dissolution features along the *c*-axis of the particles (Figure 9a). We occasionally observed the presence of pyramid-shaped dissolution pits, located on planes that intersect [001] (Figure 9b). Several particles showed rounded boundaries (Figure 9c) and irregular surfaces (Figure 9d). These observations are similar to those made by Rozalen et al. [39], who observed the development of kinks along the length of the fibers and coalescence of etch pits perpendicular to the *c*-axis. Our observations indicate that, on a qualitative basis, shorter non-fibrous particles appear to show a more pronounced dissolution along the *c*-axis.

3.12. Dimensional Results Obtained by FE-ESEM for the Material after Dissolution Experiment

Determination of the dimensions for the material after it had interacted for 168 h with Gamble's solution (Table 6) was performed the same way as before the experiment.

After the dissolution experiment, the sample exhibits a larger dimensional range and higher standard deviations for most of the measured parameters compared to before the experiment. Exceptions to this trend are seen for the $10^2\times$ w range and standard deviation and for the $10^4\times$ L and standard deviation.

The proportions of the different habits in the powder after the dissolution experiment (Table 7) are different from those retrieved for the starting material (Table 4). However, fibers still predominate at a magnification of $10^2\times$, whereas bladed habits predominate at higher magnifications.

After interaction with Gamble's solution, the percentage of EMPs in the sample is different compared to the sample before the dissolution experiment at each magnification: the proportion of EMPs increased from 54.00% to 67.33% at $10^2\times$ and from 2.00% to 12% at $10^4\times$, whereas it decreased from 47.33% to 42.00% at a magnification of $10^3\times$ (see full dimensional dataset and additional graphical representation in the Supplementary Materials, S1). Considering all three magnifications together, the overall proportion of EMPs is larger by 18% in the sample after the dissolution experiment relative to the starting material.

3.13. Estimation of Fiber Biodurability

Biopersistence describes the capability of a mineral particle to persist in the human body while subject to physical, chemical, and physiological mechanisms of clearance [40].

Whereas our experimental setup does not allow for a quantitative determination of biopersistence, it is possible to quantify the biodurability of the mineral particles; i.e., their resistance to chemical alteration. Biodurability, which contributes to biopersistence, can be calculated by using the following equation [41,42]:

$$t = \frac{3}{4} \cdot \frac{w}{RV_m} \quad (3)$$

where w is the particle width (m), R is the dissolution rate (mol·m^{-2}·s^{-1}), and V_m is the molar volume of the particles (m^3·mol^{-1}).

We thus calculated the particle biodurability starting from the smallest measured diameter (0.05 μm) to a maximum diameter of 3 μm (Figure 10).

The smallest particle (0.05 μm) dissolves in 3.6 ± 2.4 years, whereas a particle with a diameter of 3 μm in 216 ± 2 years. The uncertainty was determined by error propagation in Formula (3).

4. Discussion

The VLM and FE-ESEM morphological observations on the original sample revealed a fibrous morphology and the occurrence of asbestiform, well-elongated individual fibers arranged in prismatic millimetric and sub-millimetric aggregates. Whereas the asbestiform units are well aligned on undisturbed surfaces, fractured areas show randomly oriented fibers. After short grinding by hand (5 min and minimal mechanical stress), the observed morphology is clearly different, with a predominance of non-asbestiform characteristics.

The combination of XRPD and EPMA data identified the sample precisely at the boundary between the ideal compositional ranges of tremolite and actinolite.

The small surface area determined by BET analysis (0.4786 ± 0.0104 m^2·g^{-1}) is compatible with our morphological observations as well as with literature data for bulk amphiboles, which were prepared in a very similar fashion (0.46 m^2·g^{-1} in [43]). The surface area determined here, however, is one order of magnitude lower than that of a nearly pure asbestiform tremolite (short fibers, surface area 9.2 m^2· g^{-1} [44]).

The dimensional analysis documents that the estimation of the average length and its distribution obtained through laser diffraction is in good agreement with the measurement performed by the FE-ESEM over three orders of magnitude. In detail, however, laser diffraction failed to properly describe the studied population, as it returned a flat edged bimodal, poorly sorted distribution (Table 2). This is most likely a consequence of the fact that laser diffraction cannot take into account the rich variety of habits that comprise the investigated powder and the presence of particle agglomerates. The FE-ESEM investigation of the crystal habit at different magnifications, on the other hand, revealed that the predominant habit is different at different magnifications (10^2×, 10^3×, and 10^4×), and therefore, we conclude that the use of a single magnification when describing a sample can result in a different distribution of both dimension and habit.

Typically, microscopically-recorded dimensional distributions fail to correctly describe the abundance of the smaller particles due to instrumental limit or observation issues [38],

superposition of particles or the reciprocal screen effect, and insufficient contrast or poor resolution at a certain magnification range. Examination of all three power-law curves obtained at $10^2\times$, $10^3\times$, and $10^4\times$ documents that the information regarding the lower end of the size distribution is enhanced, which results in a higher frequency of small particles compared to the one detected at lower magnifications. Inspection of the fractal model chart reveals that the observations made at $10^4\times$ complement those made at lower magnifications ($10^2\times$, $10^3\times$), including particles with $L < 6$ μm. On the other hand, the $10^4\times$ data fail to describe the longest particles present in the population. The overlap between the $10^2\times$ and the $10^3\times$ data is larger than the overlap between the $10^3\times$ and $10^4\times$ data.

The fractal model yields a good fit ($R^2 \geq 0.90$) for all three studied distributions, where the resulting fractal dimensions are similar and within the calculated standard error. The slight tendency of D to decrease with increasing magnification can be due to the fact that we investigated a complex powder in which each individual habit contributes at different magnifications. A lower value of D is compatible with a lower resistance to fracture, which is expected for particles that can easily be separated mostly along the elongation axis. The fractal dimension calculated at 10^4x is very similar to the one calculated by Wylie [38] for a tremolite from California with $\beta < 3{:}1$, investigated by SEM ($D = 2.13$), but slightly higher than the one of another Californian tremolite, which exhibits an aspect ratio >3:1 ($D = 1.70$). Wylie [38] further reported identical D values of 1.42 for two Korean tremolite samples, one with $\beta < 3{:}1$, the other with $\beta > 3{:}1$. These results thus document that a given mineral from different outcrops may show a different fracture resistance, regardless of its morphology. In general, however, the fibrous variety of a given mineral has a smaller D value than the non-fibrous counterpart [38]. Overall, our data suggest that combining descriptive statistics with a fractal model over different magnification ranges is more effective in describing a complex particle population than observation and counting made at a fixed magnification for a given number of fields of view. The descriptive statistics and the fractal model are compatible, and they may be applied together.

Regulations from different countries commonly define asbestos fibers by a certain length, width, and β. When we change magnification, both the average β values and the A_{real}/A_{calc} values remain similar. However, individual L, w, A_{real} and $A_{calculated}$ values change according to the selected magnification. This observation can lead to problems with the application of different microscopy techniques or methods for evaluating the presence of regulated fibers (e.g., moving from VLM to SEM, or even to TEM). This is also true when the magnification is changed during the observation, as shown by our fractal model and in accordance with Wylie [38], who compared VLM, SEM and TEM. The use of a fractal approach should help in closing the gap in information generated using a single instrument with a fixed magnification, where it is assumed that the observed particles are the product of a scale-invariant phenomenon.

The dimensional term "s" is theoretically the best mono-dimensional descriptor of a particle's projected area [34]. A limitation exists, however, when an investigator wants to assess the potential toxicity or breathability of a powder using this dimension, since there is no published investigation on this topic. The term "s" can be substituted by D_{ae}, which is a mono-dimensional term describing the 3-dimensionality of the particles, which takes into

account the ratio between the major dimensions (*L* and *w*). This term can be used to describe the aerodynamic behavior of the particles in the environment (e.g., air) as well as their deposition in the human body (e.g., lungs). After the interaction with Gamble's solution, we recorded a general increase in the range of most dimensional parameters and their σ_{n-1} values. The dissolution process, thus, not only generated new particles in the smallest dimensional categories, but also led to the formation of particles in the larger categories. In fact, large non-measurable particles (data not reported in the statistical summary) were visible at $10^2\times$ in the original starting material, and we believe that these particles may be responsible for the larger particles observed in the sample after its interaction with Gamble's solution. This somewhat counterintuitive effect of dissolution on the particle population makes a differential study across different magnifications even more important.

Furthermore, after interaction with Gamble's solution, the morphology of the particles is different. Overall, the dominant habit is the same before and after the interaction, but their percentages changed slightly: fibers increased by 1.33% at $10^2\times$, becoming the dominant habit; bladed particles increased by 4.00% at $10^3\times$, and remained the dominant habit; bladed particles decreased by 3.33% at $10^4\times$, but also remained the dominant habit. These modifications seem to be more intense for shorter particles, possibly as a consequence of a suspected higher number of defects along the *c*-axis of non-asbestiform amphiboles. Particles occasionally show deeply striated and stepped surfaces, probably indicating that the dissolution proceeded selectively between the I-beams of the amphibole structure and not just on planes intersecting the *c*-axis.

The last dimensionally related aspect of particular importance is related to the percentage of EMPs according to the NIOSH classification [37]. We have shown here that changing magnification from $10^2\times$ to $10^4\times$ led to a reduction of the percentage of EMPs from 54.00% to 2.00% in the starting material, and from 67.33% to 12.00% in the sample after the dissolution experiment. In addition, the interaction of the particle population with Gamble's solution led to an increase in the percentage of NIOSH-classified EMPs by 13.33% at $10^2\times$ and by 10.00% at $10^4\times$, but to a 5.33% decrease at $10^3\times$. Again, when considering all magnifications, there was an overall increase of EMPs by 18.00% when comparing the powdered materials before and after the experiment.

Our dissolution experiment showed that Si and Mg were released into Gamble's solution at the same rate in the first 48 h. For longer exposures (96–168 h), a nearly congruent dissolution was observed. These two elements maintained a similar bulk ratio in the solid before and after 168 h of interaction, and their ratio in solution is only slightly lower, although the difference is statistically not significant. A similar dissolution study of an actinolite-rich sample, which contained considerable amounts of chlorite and other phases, was conducted by Critelli et al. [43]. These authors showed that at near-neutral pH, chlorite had a dissolution rate that was slightly higher than that of actinolite (with partially overlapping error bars). Therefore, some of the Mg and Si detected in our own dissolution experiment might have been derived from the small amounts of chlorite (estimated at 2 wt. % by XRPD). However, the potential contribution from chlorite dissolution is probably very small in our case.

The calculated Si-release rate for the first 48 h ($1.21 \times 10^{-12} \pm 1.13 \times 10^{-13}$ mol·m^{-2}·s^{-1}) is one order of magnitude smaller than the one calculated for tremolite in the experiment by Critelli et al. (3.6×10^{-11} mol·m^{-2}·s^{-1}, [43]). The slower dissolution observed in our study is likely related to the smaller surface area (about one order of magnitude smaller) and to the fact that Gamble's solution is likely to reach saturation faster than the buffer solution used in the cited work. Alternatively, this may be simply due to the different experimental conditions.

Another interesting result of our experiment is that the Ca concentration in solution increased strongly in the first 24 h, but decreased subsequently. This decrease could be due to recrystallization and settling of Ca-bearing particles, which we did indeed observe at a micrometer/sub-micrometer scale (data not shown). Similarly, Ca-phosphate precipitation on the surface of crocidolite fibers was observed by Pacella et al. [45]. The Fe was barely released into the solution at the chosen experimental conditions. According to the literature, Fe most likely rearranges itself into new structures with lower coordination geometry while being oxidized at the surface of the particles (e.g., [45]).

Notably, in our experiment no Al release was detected. Therefore, and because our sample is almost entirely composed of tremolitic amphibole, with a very small amount of chlorite (2 wt. %), we conclude that the released elements are derived almost exclusively from the dissolving tremolitic amphibole.

The calculated biodurability values allow us to speculate that the studied mineral may be characterized by a long biopersistence in the human body. The particle population studied here, however, shows a shorter lifetime than a tremolite examined in similar conditions [42]. Rozalen et al. [42] have shown that a fiber of 0.1 μm in diameter dissolves at pH 7.4 in 92 years, whereas in our case a fiber of 0.1 μm in similar conditions has a lifetime of 72 ± 2 years.

5. Conclusions

The applied multi-analytical approach provided complementary details for the characterization of the studied tremolitic amphibole. Overall, the results from different methods are in good agreement. The dimensional investigation revealed that new models should be applied to more completely describe a particle population in its entire dimensional range and that a fractal model could help, but further investigations involving multiple particle populations are needed. The large variation in dimensions and habits at different magnifications, together with the increased proportion of EMPs (according to the NIOSH definition) after our dissolution experiments, suggests that the regulatory body could improve its methods by including counting at multiple magnifications as well as a fractal model together with descriptive statistics. The species released into solution might play some role in different bio-compartments. We think that for a better understanding of the related toxic mechanisms, the physical, structural, and chemical properties of the fibers and the newly generated phases have to be determined in detail for both asbestiform minerals and other minerals with similar properties, which may occur in the same sample. This, together with the calculated fiber lifetime, is particularly important when attempting to

describe the early phase of the mechanism(s) that can lead to mineral-related disease and its evolution over longer periods.

Supplementary Material

Refer to Web version on PubMed Central for supplementary material.

Acknowledgments:

The authors are grateful to the Associazione Micro-mineralogica Italiana (AMI) members Marco Ciriotti and Vincenzo Miletto that kindly provided the studied samples. We thank Erica Bittarello for help with μRaman spectrum image. We thank M. Serracino for kindly assisting with collecting the EPMA data.

Funding: This study was supported by grants P30-ES013508 and P42ES023720 awarded by the NationalInstitute of Environmental Health Sciences (NIEHS). The findings are not the official opinions of NIEHS or NIH.The Grant to Department of Science, Roma Tre University (MIUR-Italy Dipartimenti di Eccellenza, ARTICOLO 1,COMMI 314–337 LEGGE 232/2016) is gratefully acknowledged. This work was carried out in part at the Singh Center for Nanotechnology, part of the National Nanotechnology Coordinated Infrastructure Program, which is supported by the National Science Foundation grant NNCI-1542153.

References

1. Gamble JF; Gibbs GW; Nolan RP An evaluation of the risk of lung cancer and mesothelioma from exposure to amphibole cleavage fragments. Regul. Toxicol. Pharmacol. 2008, 52, S154–S186. [PubMed: 18396365]
2. Gualtieri AF (Ed.) Introduction In Mineral Fibres: Crystal Chemistry, Chemical-Physical Properties, Biological Interaction and Toxicity (EMU Notes in Mineralogy); European Mineralogical Union: London, UK, 2017; Volume 18, pp. 1–15. ISBN 9780903056656.
3. Ferro A; Zebedeo CN; Davis C; Ng KW; Pfau JC Amphibole, but not chrysotile, asbestos induces anti-nuclear autoantibodies and IL-17 in C57BL/6 mice. J. Immunotoxicol. 2014, 11, 283–290. [PubMed: 24164284]
4. Pfau JC; Serve KM; Noonan CW Autoimmunity and asbestos exposure. Autoimmune Dis. 2014, 2014, 782045. [PubMed: 24876951]
5. Meeker GP; Bern AM; Brownfield IK; Lowers HA; Sutley SJ; Hoefen TM; Vance JS The composition and morphology of amphiboles from the Rainy Creek complex, near Libby, Montana. *Am. Mineral.* 2003, 88, 1955–1969.
6. Boulanger M; Morlais F; Bouvier V; Galateau-Salle F; Guittet L; Maquignon M; Paris C; Raffaelli C; Launoy G; Clin B O32–1 Digestive cancers and occupational asbestos exposure: Significant associations in a French cohort of asbestos plant workers. *Occup. Environ. Med.* 2016, 73, A58.
7. Clin B; Thaon I; Boulanger M; Brochard P; Chamming's S; Gislard A; Lacourt A; Luc A; Ogier G;Paris C; Pairon J Cancer of the esophagus and asbestos exposure. *Am. J. Ind. Med.* 2017, 60, 968–975. [PubMed: 28884469]
8. Di Ciaula A Asbestos ingestion and gastrointestinal cancer: A possible underestimated hazard. *Expert Rev. Gastroenterol. Hepatol.* 2017, 11, 419–425. [PubMed: 28276807]
9. Paris C; Thaon I; Hérin F; Clin B; Lacourt A; Luc A; Coureau G; Brochard P; Chamming's S; Gislard A; et al. Occupational asbestos exposure and incidence of colon and rectal cancers in French men:The asbestos-related diseases cohort (ARDCo-Nut). *Environ. Health Perspect.* 2017, 3, 409–415.
10. Gunter ME; Belluso E; Mottana A Amphiboles: Environmental and health concerns.Rev. Mineral. Geochem 2007, 67, 453–516.
11. Martin RF Amphiboles in the igneous environment. Rev. Mineral. Geochem 2007, 67, 323–358.
12. Schumacher JC Metamorphic amphiboles: Composition and coexistence. Rev. Mineral. Geochem. 2007, 67, 359–416.
13. Vignaroli G; Rossetti F; Belardi G; Billi A Linking rock fabric to fibrous mineralisation: A basic tool for the asbestos hazard. Nat. Hazard Earth Syst. 2011, 11, 1267–1280.

14. Vignaroli G; Ballirano P; Belardi G; Rossetti F Asbestos fibre identification vs. evaluation of asbestos hazard in ophiolitic rock mélanges; a case study from the Ligurian Alps (Italy). *Environ. Earth Sci*. 2014, 72, 3679–3698.
15. Trommsdorff V; Montrasio A; Hermann J; Müntener O; Spillman P; Gieré R The geological map of Valmalenco. *Schweiz. Mineral. Petrogr. Mitt*. 2005, 85, 1–13.
16. Trommsdorff V; Evans BW Antigorite-ophicarbonates: Contact metamorphism in Valmalenco, Italy. *Contrib. Mineral. Petrol*. 1977, 62, 301–312.
17. Hermann J; Müntener O; Trommsdorff V; Hansmann W; Piccardo GB Fossil crust-to-mantle transition, Val Malenco (Italian Alps). J. Geophys. Res-Solid Earth 1997, 102, 20123–20132.
18. Bocchio R; Diella V; Adamo I; Marinoni N Mineralogical characterization of the gem-variety pink clinozoisite from Val Malenco, Central Alps, Italy. Rend. Fis. Acc. Lincei 2017, 28, 549–557.
19. Trommsdorff V; Evans BW Titanian hydroxyl-clinohumite: Formation and breakdown in antigorite rocks (Malenco, Italy). *Contrib. Mineral. Petrol*. 1980, 72, 229–242.
20. Wojydr M Fityk: A general purpose peak fitting program. *J. Appl. Crystallogr*. 2010, 42, 1126–1128.
21. Marques MRC; Loebenberg R; Almukainzi M Simulated biological fluids with possible application in dissolution testing. Dissolut. Technol. 2011, 18, 15–28.
22. Pacella A; Fantauzzi M; Turci F; Cremisini C; Montereali MR; Nardi E; Atzei D; Rossi A; Andreozzi GB Dissolution reaction and surface iron speciation of UICC crocidolite in buffered solution at pH 7.4: A combined ICP-OES, XPS and TEM investigation. Geochim. Cosmochim. Acta 2014, 127, 221–232.
23. Della Ventura G; Vigliaturo R; Gieré R; Pollastri S; Gualtieri AF; Iezzi G Infrared spectroscopy of the regulated asbestos amphiboles. Minerals 2018, 8, 413.
24. Oberti R; Cannillo E; Toscani G How to name amphiboles after the IMA 2012 report: Rules of thumb and a new PC program for monoclinic amphiboles. Periodico Mineral 2012, 81, 257–267.
25. Locock AJ An Excel spreadsheet to classify chemical analyses of amphiboles following the IMA 2012 recommendations. Comput. Geosci 2014, 62, 1–11.
26. Hawthorne FC; Oberti R; Harlow GE; Maresch WV; Martin RF; Schumacher JC; Welch M IMA Report: Nomenclature of the amphibole supergroup. *Am. Mineral*. 2012, 9, 2031–2048.
27. Leake BE; Woolley AR; Arps CE; Birch WD; Gilbert MC; Grice JD; Hawthorne FC; Kisch HJ; Krivovichev VG Nomenclature of amphiboles: Report of the subcommittee on amphiboles of the International Mineralogical Association commission on new minerals and mineral names. Mineral. Mag 1997, 61, 295–321.
28. Leake BE; Woolley AR; Birch WD; Burke EA; Ferraris G; Grice JD; Hawthorne FC; Kisch HJ; Krivovichev VG; Schumacher JC; et al. Nomenclature of amphiboles: Additions and revisions to the International Mineralogical Associations amphibole nomenclature. Mineral. Mag 2004, 68, 209–215.
29. Lucci F; Della Ventura G; Conte A; Nazzari M; Scarlato P Naturally Occurring Asbestos (NOA) in Granitoid Rocks, A Case Study from Sardinia (Italy). Minerals 2018, 8, 442.
30. Rinaudo C; Belluso E; Gastaldi D Assessment of the use of Raman spectroscopy for the determination of amphibole asbestos. *Mineral. Mag*. 2004, 68, 455–465.
31. Apopei AI; Buzgar N; Buzatu A Raman and infrared spectroscopy of kaersutite and certain common amphiboles. Analele Stiintifice ale Universitatii “Al. I. Cuza” din Iasi. Seria Geologie 2011, 57, 35–58.
32. Della Ventura G The analysis of asbestos minerals using vibrational spectroscopies (FTIR, Raman): Crystal Chemistry, identification and environmental applications In Mineral Fibres: Crystal Chemistry, Chemical-Physical Properties, Biological Interaction and Toxicity (EMU Notes in Mineralogy); Gualtieri AF, Ed.; European Mineralogical Union: London, UK, 2017; Volume 18, pp. 135–169. ISBN 9780903056656.
33. Ishida K; Jenkins DM; Hawthorne FC Mid-IR bands of synthetic calcic amphiboles of tremolite-pargasite series and of natural calcic amphiboles. Am. Mineral. 2008, 93, 1112–1118.
34. Kouropis-Agalou K; Liscio A; Treossi E; Ortolani L; Pugno NM; Palermo V Fragmentation and exfoliation of 2-dimensional materials: A statistical approach. Nanoscale 2014, 6, 5926–5933. [PubMed: 24759898]

35. Gonda I; Abd El Khalik AF On the calculation of aerodynamic diameters of fibers. *Aerosol Sci. Technol.* 1985, 4, 233–238.
36. Veblen DR; Wylie AG Mineralogy of amphiboles and 1:1 layer silicates In Reviews in Mineralogy and Geochemistry; Guthrie GD Jr., Mossman BT, Eds.; Mineralogical Society of America: Chantilly, VA, USA, 1993; Volume 28, pp. 61–137. ISSN 0275–0279.
37. National Institute for Occupational Safety and Health (NIOSH). *Asbestos Fibers and Other Elongated Mineral Particles: State of the Science and Roadmap for Research*; DHHS Publication No.2011–159; 2011 Available online: https://www.cdc.gov/niosh/docs/2011-159/pdfs/2011-159.pdf (accessed on 28 November 2018).
38. Wylie AG Modeling asbestos population: A fractal approach. Canad. Mineral. 1993, 30, 437–446.
39. Rozalen M; Ramos ME; Gervilla F; Kerestedjian T; Fiore S; Huertas FJ Dissolution study of tremolite and anthophyllite: pH effect on the reaction kinetics. Appl. Geochem. 2014, 49, 46–56.
40. Bernstein DM; Castranova V; Donaldson K; Fubini B; Hadley J; Hesterberg T; Kaneg A; Laih D; McConnell EE; Muhle H; et al. Testing of fibrous particles: Short-term assays and strategies. Inhal. Toxicol 2005, 17, 497–537. [PubMed: 16040559]
41. Hume LA; Rimstidt JD The biodurability of chrysotile asbestos. *Am. Mineral.* 1992, 77, 1125–1128.
42. Rozalen M; Ramos ME; Huertas FJ; Fiore S; Gervilla F Dissolution kinetics and biodurability of tremolite particles in mimicked lung fluids: Effect of citrate and oxalate. *J. Asian Earth Sci.* 2013, 77, 318–326.
43. Critelli T; Marini L; Schott J; Mavromatis V; Apollaro C; Rinder T; De Rosa R; Oelkers EH Dissolution rates of actinolite and chlorite from a whole-rock experimental study of metabasalt dissolution from $2 \leq pH \leq 12$ at 25 °C. *Chem. Geol.* 2014, 390, 100–108.
44. Pollastri S; Gualtieri AF; Lasinantti Gualtieri M; Hanuskova M; Cavallo A; Gaudino G The zeta potential of mineral fibres. *J. Hazard. Mater.* 2014, 276, 469–479. [PubMed: 24929786]
45. Pacella A; Fantauzzi M; Turci F; Cremisini C; Montereali MR; Nardi E; Atzei D; Rossi A; Andreozzi GB Surface alteration mechanism and topochemistry of iron in tremolite asbestos: A step toward understanding the potential hazard of amphibole asbestos. *Chem. Geol.* 2015, 405, 28–38.

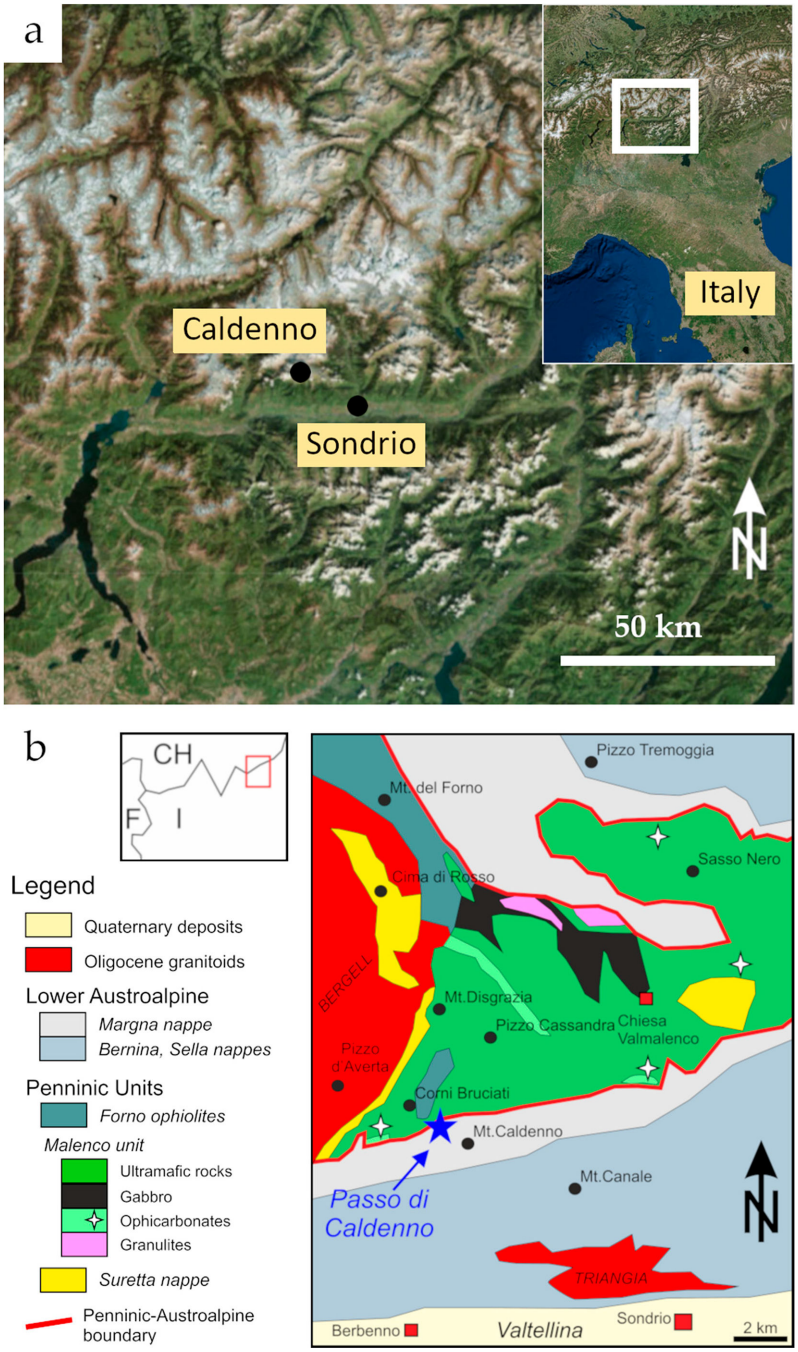

Figure 1.

(**a**) Map of area of study (Sources: Esri; DigitalGlobe, GeoEye, Earthstar Geographics, CNES/Airbus DS, USDA, USGS, AeroGRID, IGN, and the GIS User Community). (**b**) Schematic geological map of study area. Red rectangle in the upper left inset indicates the area shown in the geological map at right. Sampling locality of Passo di Caldenno shown as blue star, redrawn after [17,18].

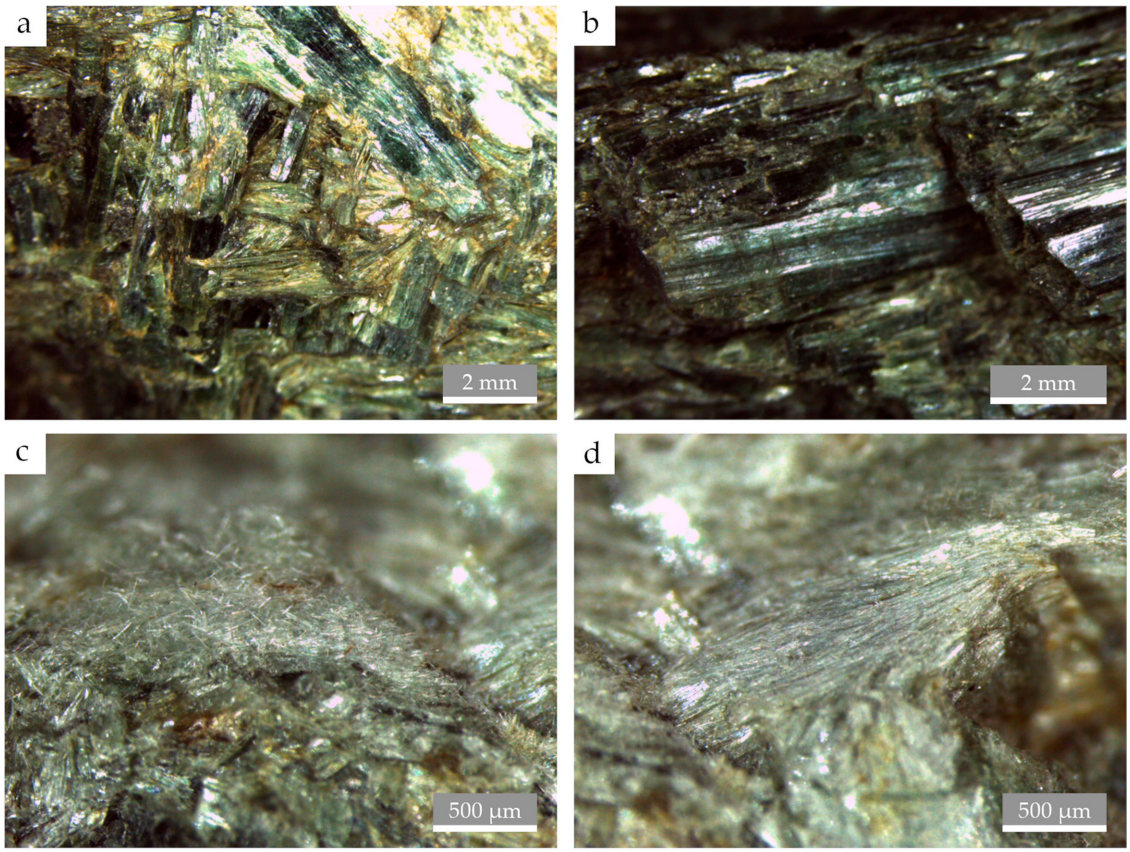

Figure 2.
Visible-light microscopic images of the studied sample from Passo di Caldenno (Sondrio, Italy): (**a**) columnar and bladed crystals; (**b**) bigger columnar crystals; (**c**) randomly oriented fibers; (**d**) parallel fibers.

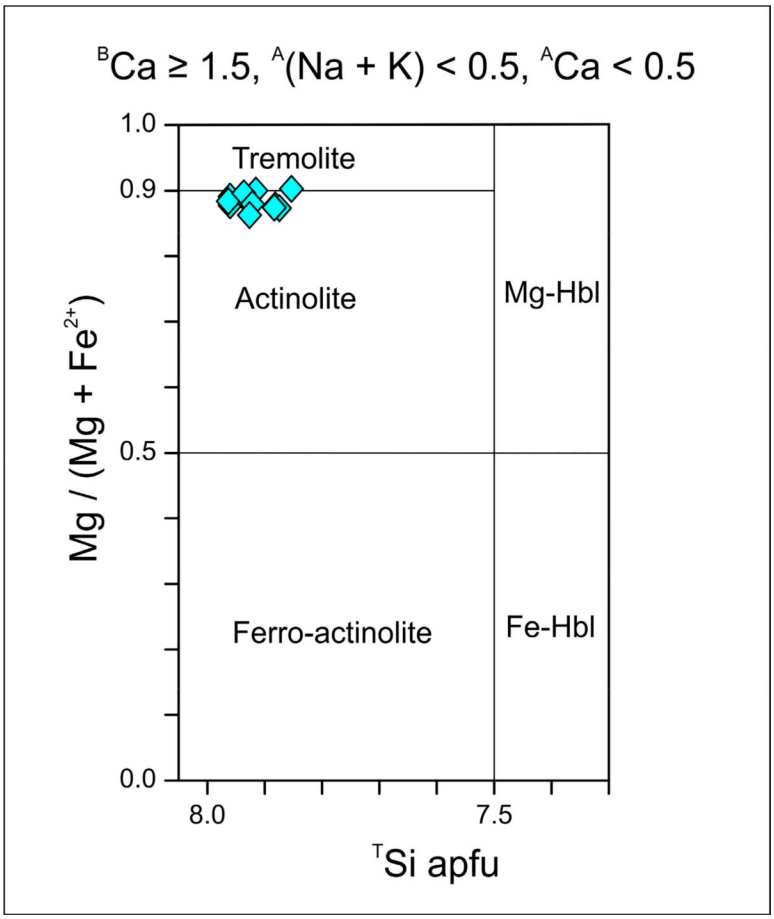

Figure 3.
Simplified classification diagram [29] showing the amphibole composition determined by EPMA (12 spot analyses). Hbl indicates hornblende.

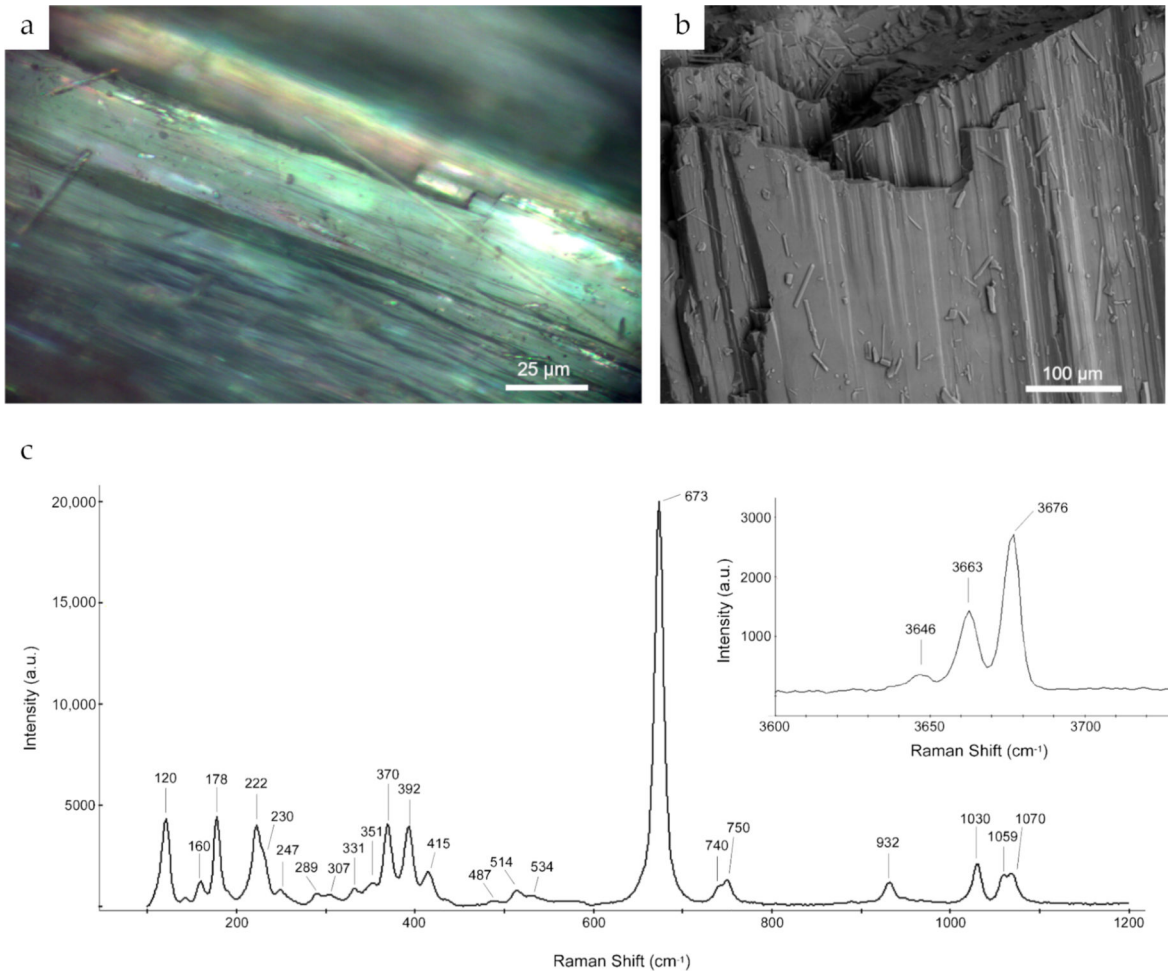

Figure 4.

Sample #S3 (**a**) green columnar aggregates analyzed by µ-Raman spectroscopy; (**b**) SE image showing the same fragment; (**c**) µ-Raman spectra in the region 100–4000 cm^{-1}.

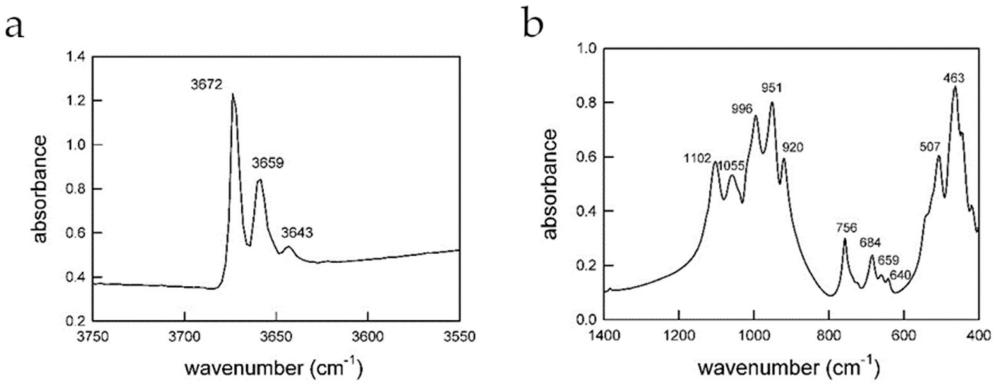

Figure 5.

(**a**) OH-stretching and (**b**) lattice mode region Fourier-transform Infrared Spectroscopy (FTIR) spectrum of the tremolitic amphibole powder from Passo di Caldenno, Italy.

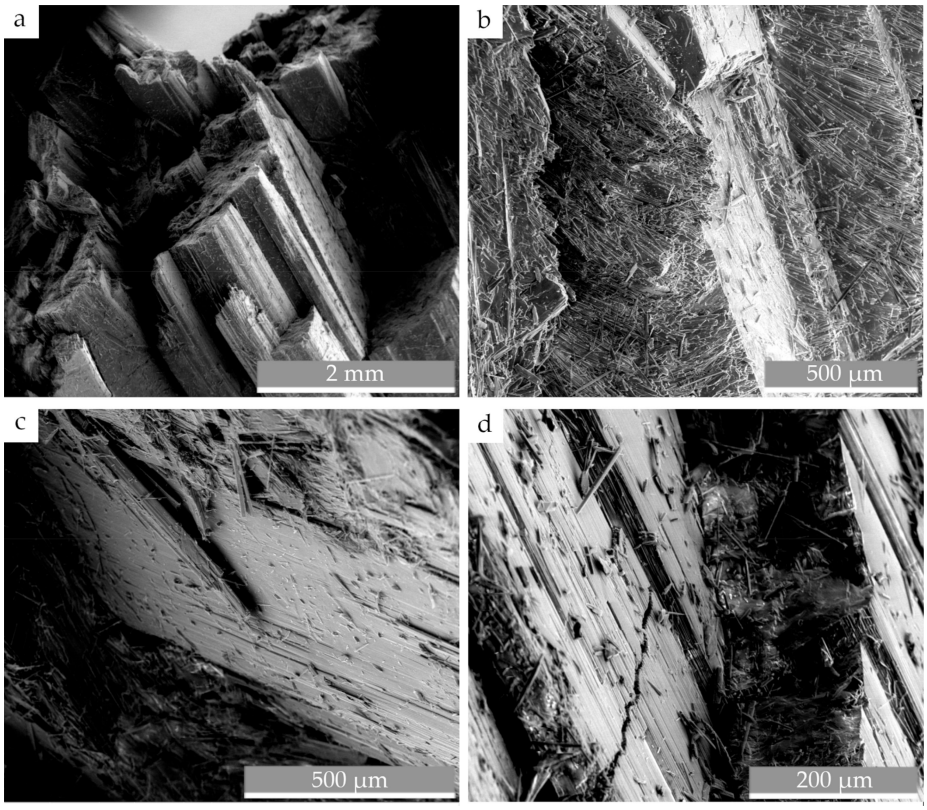

Figure 6.

SE images of the asbestiform arrangement of fibers, with some randomly oriented regions at different magnifications. (**a**) Parallel fibers in a columnar arrangement. (**b**) Parallel and randomly oriented fibers. (**c**) Fibers that appear to be detaching from the bulk. (**d**) Fracture area with randomly oriented fibers and visible asbestiform fibers.

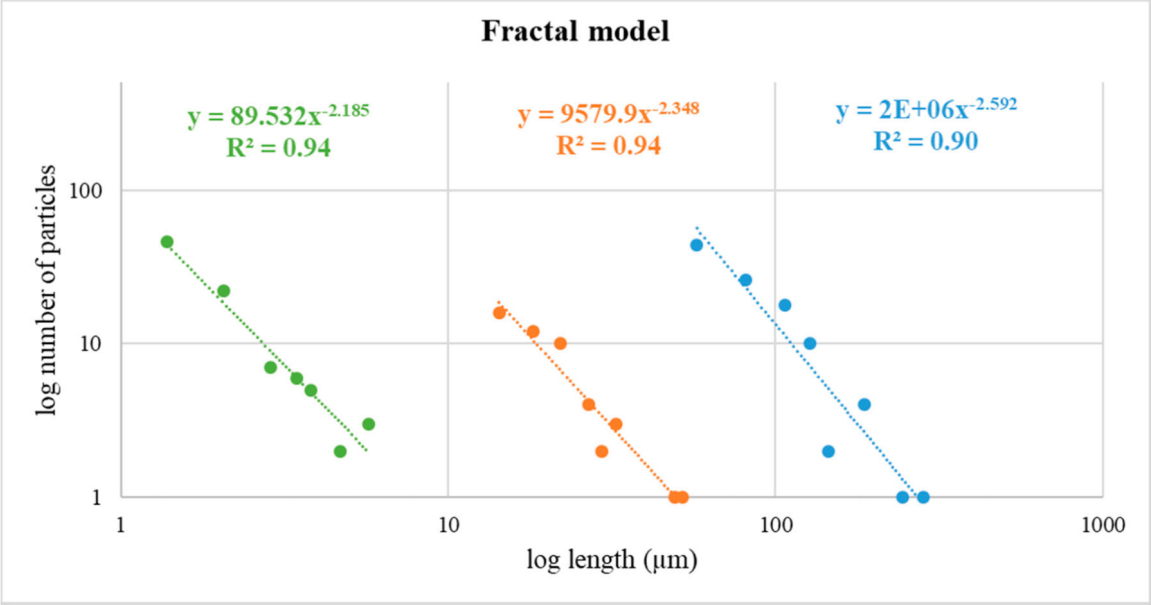

Figure 7.
Chart showing the power-law fitting of the experimental data points obtained at magnifications of $10^2\times$ (blue circles), $10^3\times$ (orange squares), and $10^4\times$ (green triangles).

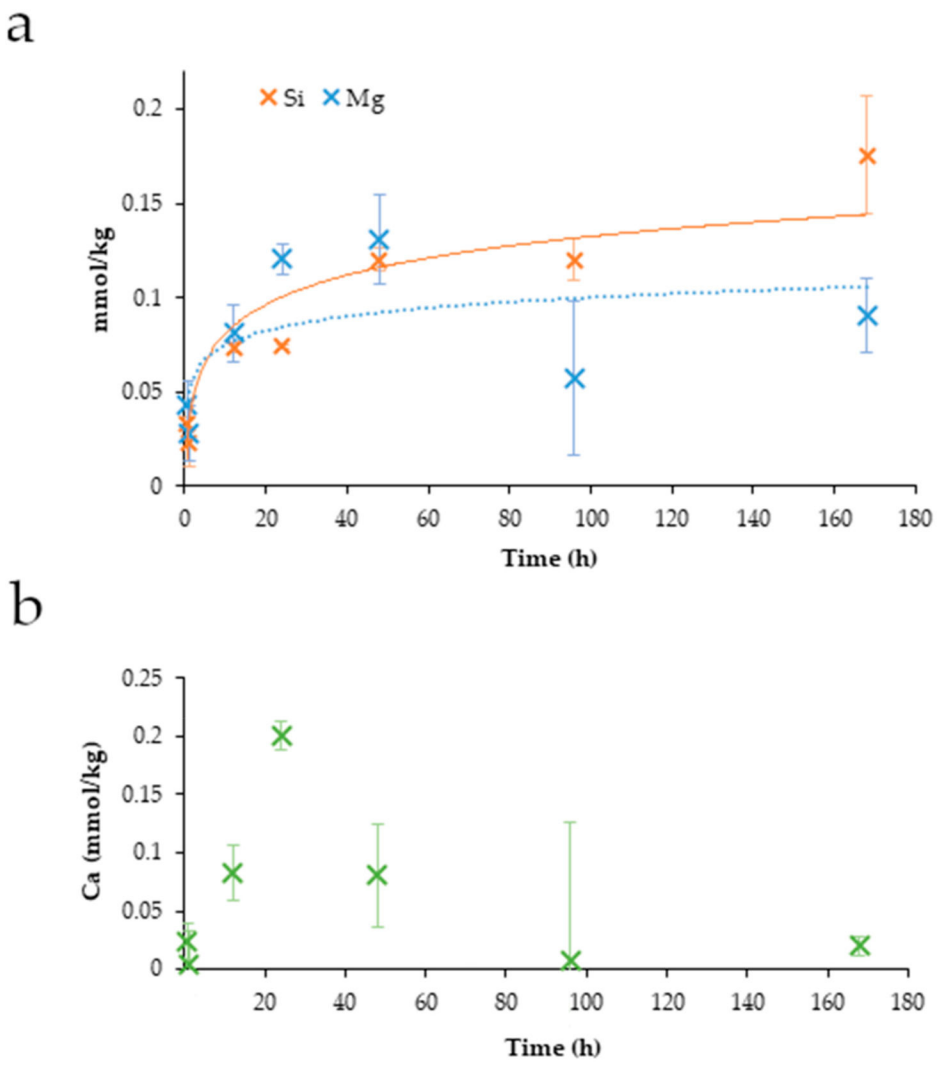

Figure 8.

Changes in the concentrations of (**a**) Si and Mg, and (**b**) Ca in Gamble's solution over time, documenting release of these elements from the powdered sample. The symbol x represents the average values, and error bars show the standard deviation of triplicate experiments.

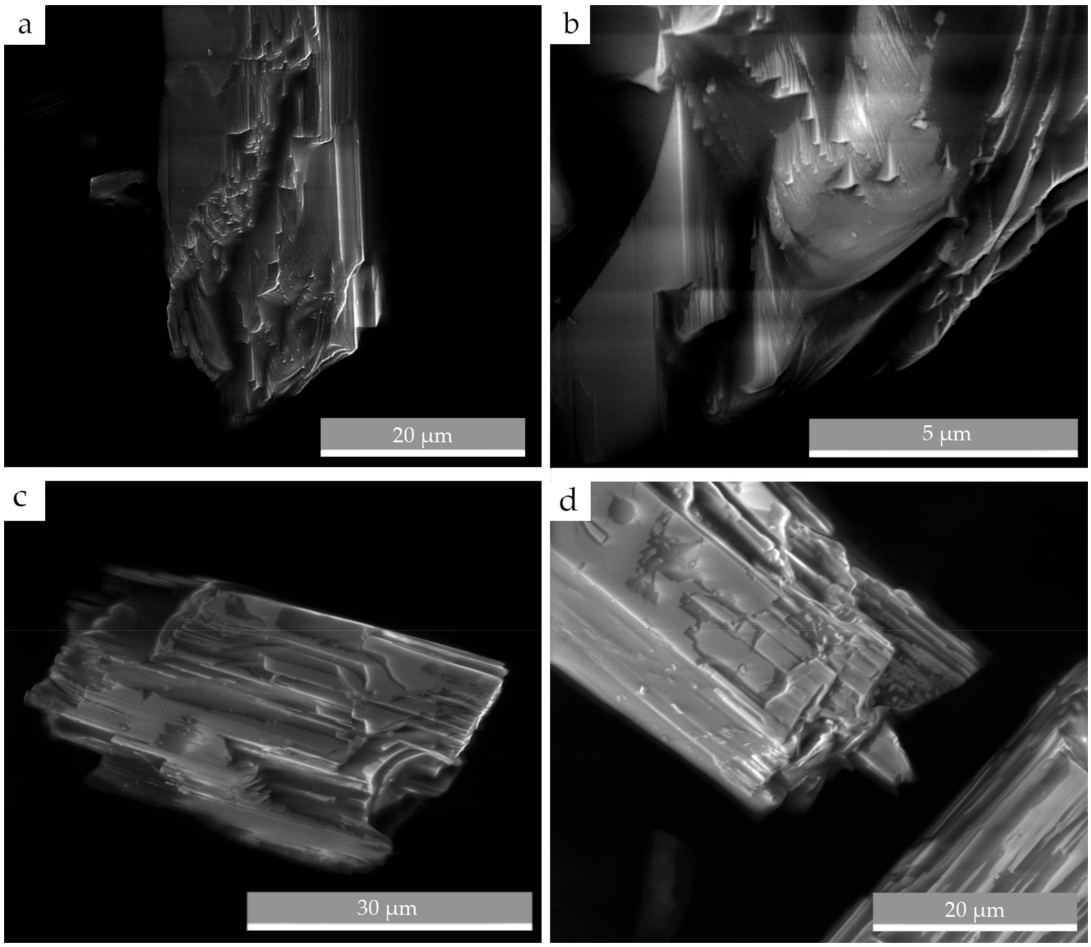

Figure 9.
Selection of SE images showing three different particles collected after 168 h of interaction with Gamble's solution. (**a**) particle with stepped, rounded, and consumed boundaries and apex, (**b**) detail of (**a**) showing rounded boundaries together with pyramid-shaped dissolution pits, (**c**) particle displaying extended rounded-boundary regions together with striated and stepped morphologies, and (**d**) particle surface with irregular cracks.

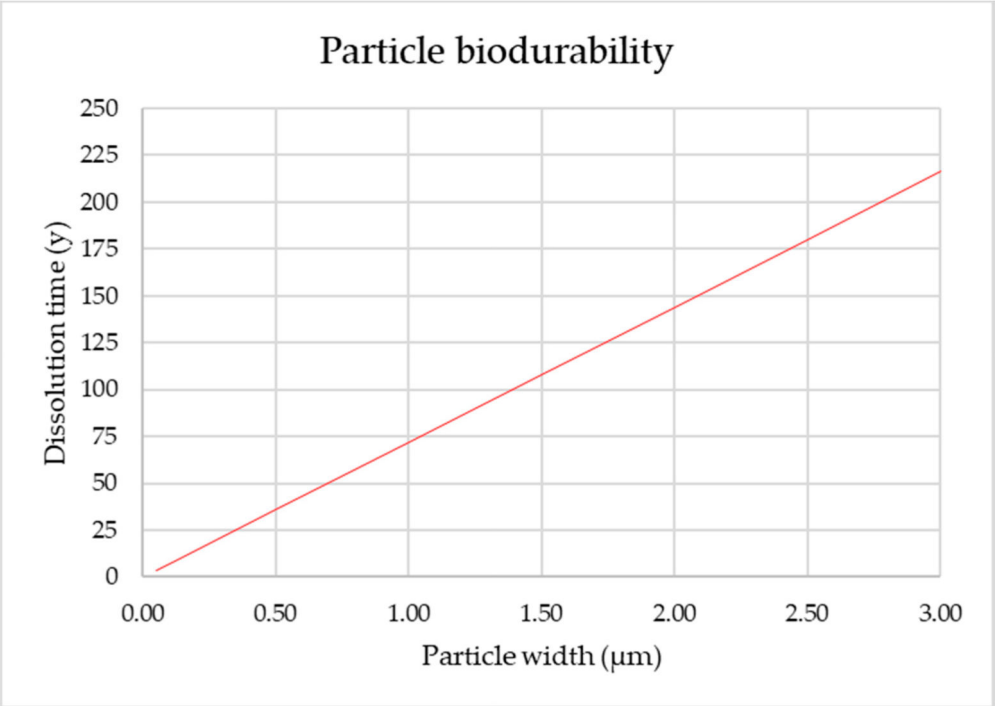

Figure 10.
Biodurability calculated for widths ranging from 0.05 µm to 3 µm. The red line represents the linear Equation (3).

Table 1.

Results from Electron Probe Micro-Analysis (EPMA).

Oxides	Average (n = 12 with σ_{n-1} in Parentheses)	*Range*
SiO_2 (wt. %)	56.68 (0.67)	*55.65–57.72*
TiO_2	<0.01	-
$Al2O_3$	0.46 (0.07)	*0.29–0.54*
FeO_t	5.37 (0.75)	*4.44–6.59*
MnO	0.19 (0.04)	*0.13–0.26*
MgO	21.16 (0.35)	*20.58–21.62*
CaO	13.12 (0.29)	*12.58–13.74*
Na_2O	0.25 (0.08)	*0.03–0.36*
K_2O	0.03 (0.02)	*0.00–0.06*
F	0.06 (0.01)	*0.00–0.22*
Cl	<0.01	-
Total	97.32	*96.47–98.16*
Normalization Scheme: 13-CNK, all ferrous iron		
Si, apfu	7.92	*7.85–7.96*
Al	0.07	*0.04–0.09*
Σ*T*	*7.99*	*7.94–8.00*
Al	0.01	*0.00–0.04*
Mn^{2+}	0.01	*0.00–0.02*
Fe^{2+}	0.58	*0.49–0.69*
Mg	4.41	*4.31–4.51*
Σ*C*	*5.00*	*5.00*
Mn^{2+}	0.02	*0.00–0.03*
Fe^{2+}	0.05	*0.00–0.12*
Ca	1.96	*1.89–1.99*
Σ*B*	*2.03*	*2.00–2.13*
Na	0.07	*0.01–0.09*
K	0.01	*0.00–0.01*
Σ*A*	0.08	*0.01–0.10*
OH	1.98	*1.90–2.00*
F	0.02	*0.00–0.10*
Σ*W*	*2.00*	*2.00*
$Mg/(Mg+Fe^{2+})$	*0.88*	*0.86–0.90*

*FeOt total iron reported as FeO. apfu: atoms per formula unit.

Table 2.

Results from laser diffraction.

Laser Diffraction Dimensional Distribution	Geometric	Logarithmic
	µm	φ
Mode 1:	127.79	2.97
Mode 2:	73.02	3.78
Mode 3:	-	-
D_{10}:	4.53	2.57
Median or D_{50}:	49.78	4.33
D_{90}:	168.75	7.79
(D_{90}/D_{10}):	37.25	3.03
(D_{90}-D_{10}):	164.22	5.22
(D_{75}/D_{25}):	6.45	1.83
(D_{75}-D_{25}):	90.44	2.69

Folk &Ward Method		
	Geometric	Logarithmic
	µm	φ
Mean	39.21	4.67
Sorting (σ)	4.13	2.05
Skewness (*Sk*)	−0.34	0.34
Kurtosis (*K*)	1.05	1.05

Table 3.

Measurements of length (*L*), width (*w*), area (A_{real}), calculated area (A_{calc}), area ratio, "*s*" dimension, and aerodynamic diameters (D_{ae}) for the powdered sample (*before* the dissolution experiment) at different magnifications.

	Magnification 10^2×(*n* = 150)							
ESEMDimensional Study	**L**	**w**	**L/w**	**A_{real}**	**A_{calc}**	**A_{real}/A_{calc}**	**s (A_{real})**	**D_{ae}**
Mean	75.03	26.00	4.53	2141.08	2396.60	0.88	38.69	54.68
Median	61.56	17.75	3.18	1061.42	1181.89	0.91	32.58	44.09
Mode	#N/D	43.50	#N/D	#N/D	#N/D	#N/D	#N/D	#N/D
Max	336.27	162.91	33.37	31031.81	31038.24	1.00	176.16	256.19
Min	16.00	1.18	0.73	21.19	25.48	0.58	4.60	3.93
Std. Dev.	47.60	24.98	4.26	3660.95	3976.48	0.10	25.47	39.57
Std. Error	3.89	2.04	0.35	298.92	324.68	0.01	2.08	3.23

	Magnification 10^3×(*n* = 150)							
	L	**w**	**L/w**	**A_{real}**	**A_{calc}**	**A_{real}/A_{calc}**	**s (A_{real})**	**D_{ae}**
Mean	11.80	3.92	5.24	57.15	66.36	0.86	5.86	8.34
Median	8.52	2.80	3.47	18.50	22.35	0.90	4.30	6.13
Mode	8.18	0.75	#N/D	#N/D	#N/D	#N/D	#N/D	#N/D
Max	54.63	23.67	33.75	1046.30	1082.56	1.00	32.35	46.28
Min	2.00	0.20	0.33	0.58	0.63	0.11	0.76	0.71
Std. Dev.	9.13	3.99	5.43	114.36	125.81	0.14	4.79	7.21
Std. Error	0.75	0.33	0.44	9.34	10.27	0.01	0.39	0.59

	Magnification 10^4×(*n* = 150)							
	L	**w**	**L/w**	**A_{real}**	**A_{calc}**	**A_{real}/A_{calc}**	**s (A_{real})**	**D_{ae}**
Mean	1.87	0.59	4.03	1.07	1.40	0.87	0.87	1.26
Median	1.29	0.47	2.52	0.53	0.60	0.89	0.72	1.03
Mode	0.92	0.41	#N/D	0.20	#N/D	#N/D	0.45	#N/D
Max	41.56	2.35	59.73	10.38	28.92	1.00	3.22	5.18
Min	0.15	0.05	0.85	0.01	0.01	0.09	0.11	0.17
Std. Dev.	3.44	0.44	5.50	1.62	2.93	0.12	0.56	0.89
Std. Error	0.28	0.04	0.45	0.13	0.24	0.01	0.05	0.07

Table 4.

Proportions of particle habits (in %) in the powdered sample (*before* the dissolution experiment) at different magnifications.

Magnification	Acicular%	Bladed%	Columnar%	Equant%	Fiber%	Massive%	Platy%	Prismatic%
10^2×	7.33	16.00	12.67	10.67	21.33	6.67	4.00	21.33
10^3×	14.00	20.67	6.67	10.00	15.33	6.00	12.00	15.33
10^4×	11.33	29.33	13.33	9.33	6.67	9.33	4.00	16.67

* Highlighted values represent the most common habits.

Table 5.

Comparison of the elemental ratios in the powdered starting material, in the remaining solid after 168-h exposure to Gamble's solution, and in Gamble's solution after 168 h of interaction. Values shown for Gamble's solution are averages of triplicates with the total error given in parentheses, whereas Energy-Dispersive X-Ray Spectroscopy (EDXS) analyses are averages of 50 individual spot analyses (total error given in parentheses).

Atomic % Ratios	Powdered Starting Material Bulk EPMA	Powdered Starting Material Bulk EDXS	Powdered Sample after 168-h Exposure (Bulk EDXS)	Gamble's Solution after 168-h Experiment (ICP-OES)
$\frac{Mg}{Si}$	0.56 (0.01)	0.63 (0.1)	0.64 (0.1)	0.51 (0.04)
$\frac{Ca}{Si}$	0.25 (0.01)	0.29 (0.07)	0.41 (0.2)	0.11 (0.03)
$\frac{Fe}{Si}$	0.08 (0.01)	0.12 (0.09)	0.22 (0.2)	0.030 (0.01)

Table 6.

Measurements of length (L), width (w), area (A_{real}), calculated area (A_{calc}), area ratio, "s" dimension, and aerodynamic diameters (D_{ae}) at different magnifications for the powdered sample (*after* the dissolution experiment).

	Magnification $10^2\times(n = 150)$							
ESEMDimensional Study	**L**	**w**	**L/w**	**A_{real}**	**A_{calc}**	**A_{real}/A_{calc}**	**s (A_{real})**	**D_{ae}**
Mean	115.18	31.09	5.34	3652.20	4201.40	0.85	52.48	72.56
Median	107.94	28.31	4.02	2762.68	3081.09	0.90	52.56	68.32
Mode	#N/D	6.25	#N/D	93.99	#N/D	#N/D	9.69	#N/D
Max	462.15	94.95	40.56	22437.60	30946.22	1.00	149.79	198.56
Min	13.52	1.40	1.06	15.63	19.87	0.12	3.95	4.28
Std. Dev.	71.68	21.77	5.15	3776.07	4436.00	0.16	30.07	43.61
Std. Error	5.85	1.78	0.42	308.31	362.20	0.01	2.46	3.56

	Magnification $10^3\times(n = 150)$							
	L	**w**	**L/w**	**A_{real}**	**A_{calc}**	**A_{real}/A_{calc}**	**s (A_{real})**	**D_{ae}**
Mean	17.70	6.12	3.72	144.19	171.05	0.85	8.95	13.22
Median	10.66	4.37	2.63	33.27	41.13	0.88	5.77	8.90
Mode	4.44	1.90	#N/D	71.60	#N/D	#N/D	8.46	#N/D
Max	154.49	41.94	34.43	2188.56	2369.54	1.00	46.78	69.59
Min	1.57	0.19	1.04	0.58	0.60	0.08	0.76	0.62
Std. Dev.	19.39	6.11	3.76	298.25	343.70	0.13	8.03	11.98
Std. Error	1.58	0.50	0.31	24.35	28.06	0.01	0.66	0.98

	Magnification $10^4\times(n = 150)$							
	L	**w**	**L/w**	**A_{real}**	**A_{calc}**	**A_{real}/A_{calc}**	**s (A_{real})**	**D_{ae}**
Mean	3.64	1.38	3.12	6.19	7.66	0.83	1.95	3.00
Median	2.73	1.15	2.27	2.71	3.17	0.86	1.65	2.45
Mode	2.30	0.15	#N/D	#N/D	#N/D	#N/D	#N/D	#N/D
Max	19.99	6.85	15.25	74.16	102.53	1.00	8.61	14.88
Min	0.14	0.02	1.11	0.00	0.01	0.11	0.03	0.06
Std. Dev.	3.34	1.14	2.39	10.55	13.38	0.15	1.55	2.41
Std. Error	0.27	0.09	0.20	0.86	1.09	0.01	0.13	0.20

Table 7.

Proportions of particle habits (in %) in the powdered sample (*after* the dissolution experiment) at different magnifications.

Magnification	Acicular%	Bladed%	Columnar%	Equant%	Fiber%	Massive%	Platy%	Prismatic%
10^2×	10.67	19.33	13.33	9.33	22.67	8.67	0.67	15.33
10^3×	10.67	24.67	10.67	12.00	14.67	8.00	4.00	15.33
10^4×	10.67	26.00	19.33	11.33	6.00	10.67	0.67	15.33

* Highlighted values represent the most common habits.